
This manuscript is a preprint and is currently under review in Journal of Glaciology. Subsequent versions of this manuscript may have slightly different content. If accepted, the final version of this manuscript will be available via the 'Peer-reviewed Publication DOI' link on the right-hand side of this webpage. Please feel free to contact any of the authors; we welcome feedback

Structural weaknesses in ice mélange revealed by high resolution ICEYE SAR imagery

William D. HARCOURT,¹ Michael G. SHAHIN,² Leigh A. STEARNS,³ Siddharth SHANKAR,⁴

¹*School of Geosciences, University of Aberdeen, Aberdeen, Scotland*

²*Department of Geology, University of Kansas, Lawrence, KS, USA*

³*Department of Earth & Environmental Sciences, University of Pennsylvania, Philadelphia, PA, USA*

⁴*Viridien, Llandudno, Wales*

Correspondence: William D. Harcourt <william.harcourt@abdn.ac.uk>

ABSTRACT. The mixture of icebergs and sea ice in tidewater glacier fjords, known as ice mélange, is postulated to impact iceberg calving directly through physical buttressing and indirectly through freshwater fluxes altering fjord circulation. In this contribution, we assess the textural characteristics of ice mélange in summer and winter at the terminus of Helheim Glacier in Greenland using high resolution (1-3 m) X-band Synthetic Aperture Radar (SAR) imagery from the ICEYE small satellite constellation. The Grey Level Co-occurrence Matrix (GLCM) and statistical variations in pixel intensity down-fjord reveal structural banding within the mélange matrix in both summer and winter. The boundary between these bands represent shear zones, demonstrating structural weaknesses in the mélange that may persist throughout the year. Furthermore, we compare two iceberg segmentation methods, texture-based vs the Segment Anything Model (SAM). Both techniques detect large (>0.1 km²) icebergs in summer when pixel variations are larger, but SAM has high iceberg detection accuracy in both seasons. The detected icebergs stabilise near the mélange shear zones, suggesting they act as the nucleus of the mélange bands and control matrix stability. Our study demonstrates the potential for using high resolution ICEYE SAR imagery for studying dynamic processes in glaciology and beyond.

28 **INTRODUCTION**

29 Since the early 2000s, the Greenland Ice Sheet (GrIS) has been losing mass at a rate of 233 Gt yr⁻¹
30 (Mouginot and others, 2019; Shepherd and others, 2020; Simonsen and others, 2021; Otosaka and others,
31 2023). Approximately 66% of this mass loss was attributed to ice discharge (e.g. calving, ice flow) between
32 1972 and 2018 (Mouginot and others, 2019), which emphasises the need to understand the relative influence
33 of competing processes influencing the stability of tidewater glaciers across the GrIS. A poorly understood
34 process is the role that ice mélange, the granular mixture of icebergs and sea ice at the termini of tidewater
35 glaciers, plays in controlling the position of the ice front over different timescales (Amundson and others,
36 2020). In winter, ice mélange consists of icebergs bound through sea ice and flows downfjord with resistance
37 by the fjord margins (rigid) (Robel, 2017; Amundson and others, 2020), whilst in summer the mélange
38 matrix is mostly composed of loose icebergs and brash ice (non-rigid) within fjords where ice discharge
39 rates are large (Amundson and others, 2010). The rigidity of the ice mélange matrix impacts the magnitude
40 of the buttressing force it can exert on tidewater glacier termini and has been observed to inhibit fracturing
41 and calving (Amundson and others, 2010; Howat and others, 2010; Burton and others, 2018), whilst sudden
42 mobilisation of a rigid mélange matrix may also act as a precursor to calving events (Xie and others, 2019;
43 Amundson and others, 2020; Cassotto and others, 2021). Further, the influx of freshwater into the fjord
44 through the basal melt of the mélange matrix can increase the heat flux towards tidewater glacier termini
45 (Davison and others, 2020) and enhance submarine melt rates. These processes are likely to vary between
46 fjords and the timescales over which they operate remain largely unknown across the GrIS (Mankoff and
47 others, 2019) yet they could be crucial in modulating discharge rates.

48 Ice mélange is a highly dynamic, fragmented and mobile phenomenon that varies over a range of
49 timescales (e.g. hours, days, weeks) and hence is difficult to monitor using traditional ground-based and
50 spaceborne sensors. This inhibits our ability to develop an improved understanding of its role in stabilising
51 tidewater glacier calving fronts. Studies investigating ice mélange dynamics are limited to using either
52 coarse resolution satellite sensors (Foga and others, 2014; Cassotto and others, 2015; Bevan and others,
53 2019), field sensors with small spatial coverage (Amundson and others, 2010; Peters and others, 2015;
54 Amundson and others, 2020; Cassotto and others, 2021), or physical models with these measurements as
55 input (Amundson and Burton, 2018; Burton and others, 2018; Xie and others, 2019). Both optical and
56 Synthetic Aperture Radar (SAR) imagery have been used to detect the presence and extent of ice mélange

57 in glacial fjords as well as those where it is absent (Foga and others, 2014; Moon and others, 2015; Fried
58 and others, 2018), but this cannot be used to assess the more complex dynamics of the mélange matrix.
59 Instead, deep learning methods have been developed to segment components of the fjord system such as ice,
60 snow, and open water (Marochov and others, 2021), with some studies now attempting to detect different
61 elements of the mélange matrix such as individual icebergs (Foga and others, 2014; Shankar and others,
62 2023), but these methods remain in their infancy. Remote sensing data has proven to be more successful
63 in quantifying the flow of ice mélange downfjord using traditional feature tracking techniques applied to
64 satellite (Amundson and Burton, 2018; Bevan and others, 2019) and ground-based (Peters and others,
65 2015; Cassotto and others, 2015; Xie and others, 2019) imagery. These measurements have been used to
66 assess mélange rigidity based on the coherence of their flow rates, and when combined with modelling based
67 on granular flow physics, they may be used to quantify the buttressing force on tidewater glacier calving
68 fronts (Burton and others, 2018; Xie and others, 2019). However, current techniques used to monitor ice
69 mélange remain insufficient to fully capture its impact on tidewater glacier discharge

70 The mélange matrix consists of ice fragments varying in size from centimetres to tens of metres, hence
71 differentiating these features within coarse resolution satellite imagery and oblique viewing time-lapse
72 sequences is difficult. Further, the flow of ice mélange is granular (Burton and others, 2018) and can
73 disintegrate quickly in response to changing atmospheric and oceanic conditions (Bevan and others, 2019),
74 therefore measurements on the order of hours to days is required to assess its impact on tidewater glacier
75 stability. Measurements of ice mélange at this scale can now be achieved using large constellations of
76 CubeSats and SmallSats that can orbit the entire globe multiple times a day and acquire imagery at
77 centimetre to metre spatial resolution. This supersedes the capabilities of constellations formed of 1-
78 3 satellites (e.g. Sentinel, Landsat) which typically have revisit periods of more than a few days and
79 spatial resolutions of 10 m or more. As of 2023, there are several optical (e.g. Planet) and SAR (e.g.
80 ICEYE, Capella, Umbra) CubeSat and SmallSat constellations in orbit that are used for Earth Observation
81 purposes. However, the ability of these sensors to map ice mélange extent, features, flow rates and rigidity
82 has not been tested, inhibiting our ability to assess their applicability to ice sheet wide monitoring of the
83 ice-ocean interface and dynamic fjord conditions.

84 In this study, we evaluate the capabilities of SAR imagery acquired from the ICEYE SmallSat constel-
85 lation (Muff and others, 2022) to map and monitor seasonal differences in ice mélange conditions at the
86 terminus of Helheim Glacier in Greenland. We focus on the ability of the ICEYE satellite constellation to

87 quantify three pertinent characteristics of ice mélange:

- 88 1. Surface characteristics and structure inferred from ICEYE SAR image texture.
- 89 2. The distribution of large icebergs in the mélange matrix detected using texture-based and deep learning
90 segmentation approaches.
- 91 3. Flow rates of ice mélange determined from feature-tracking techniques to infer rigidity.

92 **STUDY SITE & DATA**

93 We study the perennial ice mélange matrix at the terminus of Helheim Glacier in southeast Greenland
94 (Figure 1). Helheim Glacier, which is the second largest contributor to total GrIS discharge (Mankoff and
95 others, 2019), flows through two branches from the north and south which coalesce into a ~ 6 km wide
96 calving front that is ~ 650 m deep and flows at ~ 20 m per day in summer. The ice mélange is sustained by
97 a constant influx of icebergs from Helheim Glacier which have residency times in the matrix of ~ 2 months
98 (Moyer and others, 2019). Modelling studies have found a weak dependence of ice mélange on buttressing
99 the Helheim Glacier calving front (Cook and others, 2014). For example, Wehrlé and others (2023) found
100 that weakening of ice mélange can enhance calving activity, but the relationship was highly dependent on
101 external forcing factors and is likely only important on short timescales. In comparison, mélange weakening
102 due to plume melting was found to not impact calving (Everett and others, 2021) but the spatial scale of
103 this process is small and neglects the larger scale fjord pattern. Atmospheric warming is also considered
104 to be a key driver of ice mélange break-up in Helheim fjord (Foga and others, 2014) through wind-driven
105 movement and surface melting. These environmental factors impact the rigidity of the ice mélange matrix
106 which can promote glacier advance when it is high but can also destabilise a calving front when the matrix
107 is loose and offers no physical support to the terminus (Miles and others, 2016).

108 We assessed the ice mélange mapping performance of ICEYE SAR imagery at Helheim Fjord in summer
109 (2021) and winter (2023) (Table 1). As of 2023, the ICEYE constellation consisted of 24 satellites (up-
110 dates here: <https://space.oscar.wmo.int/satellites/view/iceye>) which enable daily and sub-daily mapping
111 of designated regions on the Earth surface. Each satellite has a SAR payload which operates at 9.65 GHz
112 (X-band) with a single channel VV polarisation and either a left or right look direction. Here, we acquired
113 SAR imagery in StripMap mode, although several other modes are available (ICEYE, 2023), which has a
114 swath width of 30×50 km and an image area of $1,500 \text{ km}^2$ across a set of incidence angles between $15\text{-}30^\circ$.

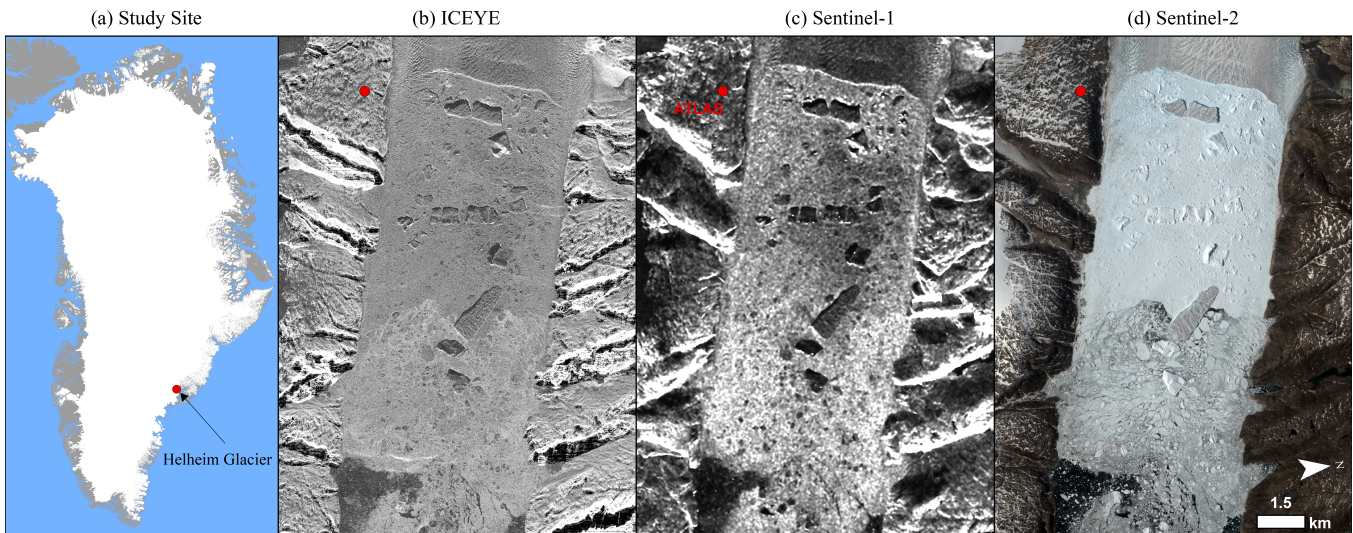


Fig. 1. (a) Location of the Helheim Glacier study site in southeast Greenland. We then show close up images of Helheim Fjord from 20th June 2021 using (b) ICEYE, (c) Sentinel-1, and (d) Sentinel-2. Red dot is the location of the ATLAS instrument.

115 The ground resolution of this product is 2.5 m. Images were acquired through tasking i.e. we acquired
 116 images at set times when the satellites were passing over Helheim Glacier and it's proglacial mélangé. In
 117 summer (2021), we acquired 3 images in one day and 2 images 7 days later (5 in total) in order to capture
 118 the sub-daily conditions of ice mélangé when it is most dynamic. In winter (2023), we acquired 10 images
 119 between 6 March 2023 and 2 April 2023, covering a period 26 days, to map the rigid structure of wintertime
 120 ice mélangé. Each image in Ground Range Detected (GRD) format was pre-processed following standard
 121 SAR processing workflows in the Sentinel Application Platform (SNAP) software by applying a speckle
 122 filter, range-doppler correction, and calibration to γ^0 . An example ICEYE image can be seen in Figure 1b
 123 and compared to a Sentinel-1 (Figure 1c) and Sentinel-2 (Figure 1d) image of the same region. The high
 124 spatial resolution of the ICEYE image enables smaller features such as fractures on the surface of icebergs
 125 to be more clearly distinguished.

126 We compared the ICEYE images to coincident Sentinel-1 scenes in Interferometric Wide (IW) mode,
 127 HH polarisation and 10 m spatial resolution. In 2021, a single Sentinel-1 image on 20 and 28 June were
 128 used for a comparison, whilst in 2023 a total of seven Sentinel-1 scenes covering the same time period as
 129 the ICEYE image acquisitions were used. To validate data products derived in this study, we used an
 130 autonomous terrestrial laser scanner (ATLAS) permanently deployed on the south side of Helheim fjord
 131 (Shahin, in prep). ATLAS scans Helheim Glacier and the ice mélangé every 6 hours during summer and
 132 once per day in winter. The primary data product is a 3D point cloud of the surface.

Table 1. Table of ICEYE SAR images used in this study.

Year	Satellite	Date	Time (UTC)	Orbit
2021	ICEYE X7	20 June	05:28:50	Descending
2021	ICEYE X8	20 June	12:54:06	Descending
2021	ICEYE X2	20 June	13:27:31	Descending
2021	ICEYE X7	28 June	05:28:43	Descending
2021	ICEYE X8	28 June	13:03:39	Descending
2023	ICEYE X12	6 March	03:51:17	Ascending
2023	ICEYE X11	8 March	04:07:35	Ascending
2023	ICEYE X8	12 March	22:54:05	Ascending
2023	ICEYE X12	14 March	03:44:19	Ascending
2023	ICEYE X11	18 March	04:04:34	Ascending
2023	ICEYE X12	21 March	03:47:52	Ascending
2023	ICEYE X11	23 March	04:01:29	Ascending
2023	ICEYE X13	27 March	03:49:20	Ascending
2023	ICEYE X2	30 March	23:29:13	Ascending
2023	ICEYE X7	2 April	15:08:06	Ascending

133 METHODS

134 Ice Mélange Segmentation

135 We first delineate the spatial extent of the ice mélange matrix by automatically calculating a threshold
136 based on the distribution of pixel values in the ocean region of the ICEYE image (Figure 2). The ocean
137 was first extracted manually using a shapefile of Sermilik Fjord (Figure 2b). The resulting backscatter
138 image of the ocean is then smoothed using a 2D Gaussian filter, after which the Otsu multi-threshold
139 method (Otsu, 1979) was applied to differentiate between the rough ice mélange matrix and homogeneous
140 ocean and sea ice pixels. In summer, two thresholds are extracted to separate the fjord into 3 zones
141 assuming ice mélange, sea ice, and open water are each present in each image. A similar approach is used
142 in winter, but initially the histogram of the fjord is extracted, lowess smoothed and the number of peaks
143 found. When the distribution is uni-modal, no threshold is applied; when the distribution is bi-modal, two
144 multi-threshold values are found using Otsu’s method; when the distribution is multi-modal with more
145 than three peaks, the standard Otsu method of finding 1 threshold is used. In both seasons, the threshold

146 inadvertently removes low backscatter pixels across the mélange such as icebergs with surface melt and the
 147 smooth surfaces of flipped icebergs (Figure 2c). This leaves behind holes in the mélange mask which we
 148 fill. Finally, features smaller than 62.5 km^2 (i.e. $2.5 \text{ m} \times 2.5 \text{ m} \times 10,000,000$ pixels) are removed in order
 149 to produce a binary image representing ice mélange and icebergs locked within sea ice (Figure 2d). This
 150 ice mélange mask is applied to both ICEYE and Sentinel-1 imagery in subsequent analysis.

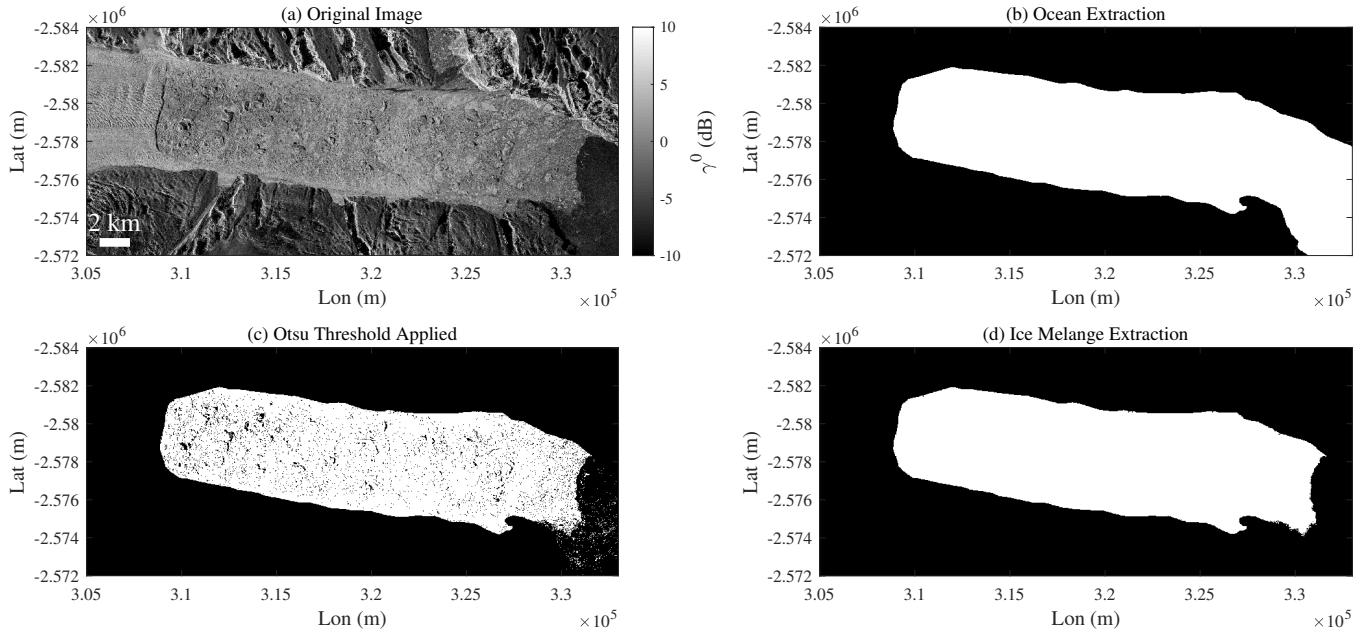


Fig. 2. Extraction of the ice mélange matrix within an ICEYE image. (a) Original ICEYE image from 30th March 2023, (b) manual extraction of the ocean area using a shapefile of Sermilik fjord, (c) application of the Otsu thresholding method, and (d) the final ice mélange matrix extracted from the data processing. In Panels (b), (c), and (d), white represents the presence of ice.

151 Texture Analysis

152 The spatial variation in pixel values across an image is defined as image texture and varies as the pixel
 153 resolution changes. The physical condition of the ice mélange surface alters radar backscatter and therefore
 154 image texture, hence analysis of texture changes over time may be used as a proxy for the state of ice
 155 mélange. Here, we quantify image texture across the ice mélange matrix in the ICEYE scenes using the
 156 following metrics:

157 *Probability Distribution Functions (PDFs):* Histograms of the ice mélange pixel values are produced
 158 for each ICEYE image to characterise the radar backscatter distribution of the ice mélange surface.

159 *Longitudinal Median Profile*: Helheim Fjord is broadly rectangular and for signal processing purposes
160 can be considered an array of pixel values. Here, we use this box array, created by first rotating the
161 image by 7° due to the angle of the fjord relative to the image acquisition, to calculate the downfjord
162 variation in radar backscatter by extracting the median value of the pixels in each column of the ice
163 mélange SAR image from the terminus of Helheim Glacier to the mélange edge.

164 *Gray Level Co-occurrence Matrix (GLCM)*: We quantify spatial patterns in pixel values by comput-
165 ing the Gray level Co-occurrence Matrix (GLCM) (Haralick and others, 1973) which calculates the
166 relationship between neighbouring pixels and maps this across the scene. We use GLCM to map the
167 ‘Correlation’ across each image, which is used to aid iceberg segmentation.

168 **Iceberg Segmentation**

169 Large ($>0.1\text{km}^2$) icebergs within ice mélange are key to bonding sea ice and brash ice together into a
170 granular matrix (Robel, 2017; Burton and others, 2018), whilst they can also act as the catalyst for mélange
171 weakening when they move (Cassotto and others, 2021; Wehrlé and others, 2023). Here, we develop two
172 methods for detecting icebergs within the noisy ice mélange environment and test the methodologies on
173 both ICEYE and Sentinel-1 scenes.

174 *Texture-based Iceberg Segmentation*

The surface features on icebergs within the ice mélange matrix have greater textural variation in the ICEYE imagery compared to Sentinel-1 (Figure 1) which motivated the development of a texture-based segmentation method to detect icebergs in mélange. We first normalised the image by dividing each pixel by the median value in the image column i.e. using the longitudinal mean profile (Figure 3b), which corrects for pixel variation downfjord. The GLCM correlation layer (Haralick and others, 1973) is then computed from this normalised mélange image (Figure 3c). In summer, iceberg edges have low GLCM correlation values as their textural variations reflect the sharp intensity boundary between the iceberg and the mélange. These edges are detected by removing high GLCM correlation values, which generates polygons with holes which are subsequently filled. In winter, this difference is not clear as the entire matrix is frozen. Therefore, to maximise the difference between icebergs and the surrounding matrix, we log-transform each pixel value in the GLCM correlation layer. A threshold is set to remove low pixel values and polygons with holes filled as before. Edges not associated with icebergs are also included in this detection process, hence we filter out

these non-iceberg features through a two-stage process. Firstly, the average thickness (T) of each feature is calculated using:

$$T = \frac{A}{L/2} \quad (1)$$

175 where A is the feature area and L is the feature perimeter length. Then, all features smaller than a
176 manually defined threshold are removed. Secondly, a bounding box around each feature is computed and
177 the density of points within it calculated in order to remove features with low pixel densities. The result
178 of this whole process is a binary image of iceberg locations.

179 *SAM Iceberg Segmentation*

180 We use the Segment Anything Model (SAM) developed by Meta to detect icebergs within the ice mélange
181 matrix (Kirillov and others, 2023). SAM is a foundational model trained on millions of images and has pre-
182 viously been shown to demonstrate good performance for detecting glaciological features such as crevasses
183 and icebergs (Shankar and others, 2023). SAM can run either with no prompts, where the model segments
184 features with no a priori information, or with prompts, whereby the user provides context on where there
185 are certain features in the scene. SAM also requires 8 bit 3 band imagery, hence we first convert our
186 ICEYE and Sentinel-1 imagery into .png files before running SAM. We also only use the HH band from the
187 Sentinel-1 imagery, since ICEYE is single channel. Here, we use no prompt SAM due to the slightly higher
188 F1 score quantified by Shankar and others (2023) for iceberg segmentation in a mélange compared to the
189 prompted score. To increase the number of icebergs segmented, we adjusted the “zoom” of our images
190 by patching each scene into 5 km x 5 km squares. Land mask artifacts can be created when adjusting
191 the “zoom”. We ignore these large artifacts, which results in misclassified segmented areas, by manually
192 filtering them out.

193 *Validation*

To quantify the accuracy of the segmentation results we compared the output of SAM with labels of icebergs that were delineated manually. We delineate a range of iceberg types within the rigid mélange matrix to achieve a diversity of sizes for validation. We did not delineate icebergs in the non-rigid matrix because there are large quantities of smaller icebergs such as growlers and bergy bits which are extremely difficult to track individually. Even for those which can be tracked there is likely to be human error leading to missed occurrences which would lead to a lower accuracy which is not representative of the methodology,

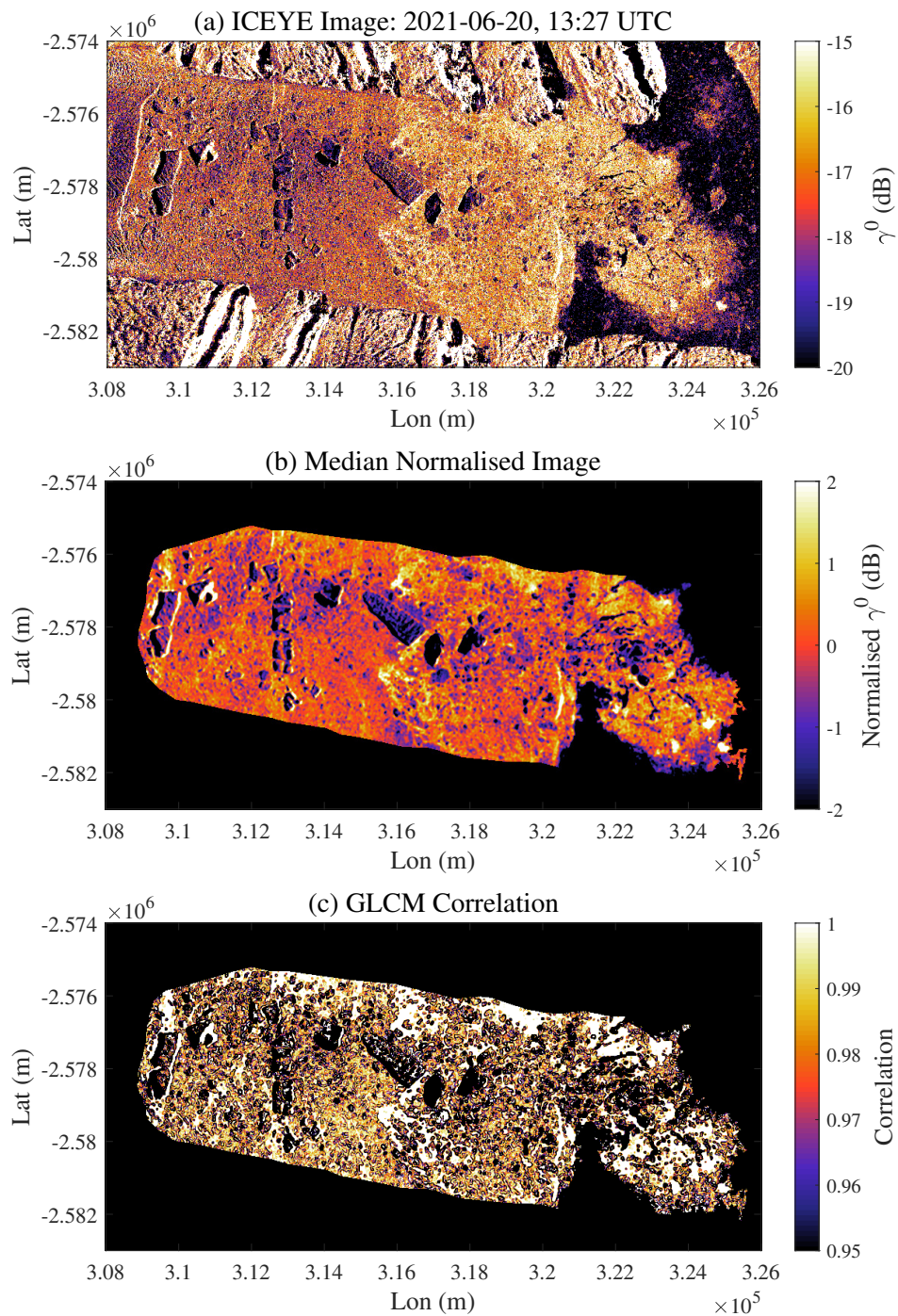


Fig. 3. (a) ICEYE image from 20 June at 13:27 UTC, colored by radar brightness. (b) Gaussian smoothed image with the ice mélangé region extracted (see section ‘Ice Mélangé Segmentation’) and normalised by the median longitudinal profile of the mélangé matrix. (c) GLCM correlation layer calculated from the normalised mélangé zone.

but rather just human bias. Comparison of the outputs to the manual labels was computed by calculating

the F1 score (Shankar and others, 2023):

$$precision = \frac{TP}{TP + FP} \quad (2)$$

$$recall = \frac{TP}{TP + FN} \quad (3)$$

$$F1 = \frac{2 \times precision \times recall}{precision + recall} \quad (4)$$

where TP is a true positive, FP is a false positive, and FN is a false negative. The F1 score ranges between 0 and 1 and is the harmonic mean of the precision and recall. The closer to 1 the F1 score is, the better the match of the SAM outputs to the manual labels and therefore the better the model performance. The F1 score for the texture-based method is unreliable due to the impact of smaller icebergs on the detection results and so this method is assessed qualitatively.

Ice Mélange Dynamics

We mapped the velocity of the proglacial mélange using the Image GeoRectification And Feature Tracking Toolbox (ImGRAFT) (Messerli and Grinsted, 2015). It was not possible to compute velocities in summer 2021 as the mélange matrix was non-rigid, hence we focus on the rigid matrix in winter 2023. The DEM used for the range-Doppler correction applied in pre-processing was set to 0 over the mélange to avoid geometric errors of an outdated DEM. Each ICEYE image was then subset to a region covering the glacier terminus, Helheim Fjord and the northern region of Sermilik Fjord. The velocities were calculated from image pairs with time differences of 2-4 days, hence we computed a total of 8 velocity maps. The images were coregistered within SNAP by stacking image pairs together. We used a template window size of 20×20 pixels and a search window size of 150×150 . The Normalised Cross Correlation (NCC) method was employed to match image features. The ICEYE velocities over the mélange matrix were validated using the velocities computed from the ATLAS 3D point clouds. Each point in the ATLAS point cloud was tracked automatically (Shahin, in prep) and the resulting displacements averaged within individual grid squares of 100×100 m, hence the final displacement map is a grid over the mélange at 100 m resolution.

213 RESULTS

214 Ice Mélange Texture

215 The texture of the ice mélange matrix in ICEYE SAR imagery differs between summer and winter (Figures
216 4 and 5). In winter, when temperatures are below freezing and the mélange matrix is more rigid, the PDFs
217 are consistently Gaussian among the 10 images with differences only in their shape, standard deviation
218 and mean value. Of the 10 winter images, the standard deviation differs by only 2.5 dB and averages at
219 13.4 dB, indicating the texture is stable over the 30 day winter study period. In comparison, the PDFs
220 for summer are much more variable. Whilst one of the mélange PDFs is Gaussian with a mean γ^0 of -17.1
221 dB, two of the PDFs are negatively skewed and another two have bi-modal distributions. The negatively
222 skewed distributions indicate that there is an increase of smaller γ^0 values in the image related to changes
223 in mélange surface characteristics. The presence of a bi-modal distribution implies that at least two regions
224 can be identified in the mélange matrix, which may be related to changes in ice density and composition.
225 The mean values of the PDFs in summer are consistently below -5 dB whilst the mean values of the
226 winter PDFs are consistently above 0 dB, providing a useful metric through which to differentiate between
227 summer and winter mélange conditions. The variation in the γ^0 distribution over 7 days illustrates the large
228 variability of ice mélange image texture in summer. In comparison, the consistent Gaussian distribution
229 in winter demonstrates that the mélange matrix maintains a random mixture of ice types over at least a
230 month.

231 There is also spatial variability in ice mélange texture as evidenced by the changes in normalised
232 median pixel values downfjord (Figure 5). These longitudinal profiles reveal zones within the mélange
233 in both summer (Figure 5a) and winter (Figure 5b). In summer, we detect 4 zones. In the first 3 km,
234 pixel values remain consistent before entering zone 2 where there is a rapid rise and plateauing of the the
235 pixel values. Zone 2 is the largest zone and extends between 3 km and 11 km from the terminus. Zone 3
236 represents the edge of the mélange and varies significantly between each image and then zone 4 represents
237 the ocean that sometimes contains ice to form part of the matrix. In comparison, we detect only two clear
238 zones in winter. The first extends from the terminus to 11 km from the terminus and is characterised
239 by a slow rise in pixel values. In Zone 2, there is a distinct change where pixel values fall at a similar
240 rate. Whilst sub-zones may exist in both summer and winter, these broad zones appear to be consistent
241 in all images in their respective seasons. There is greater spatial variability in summer compared to winter

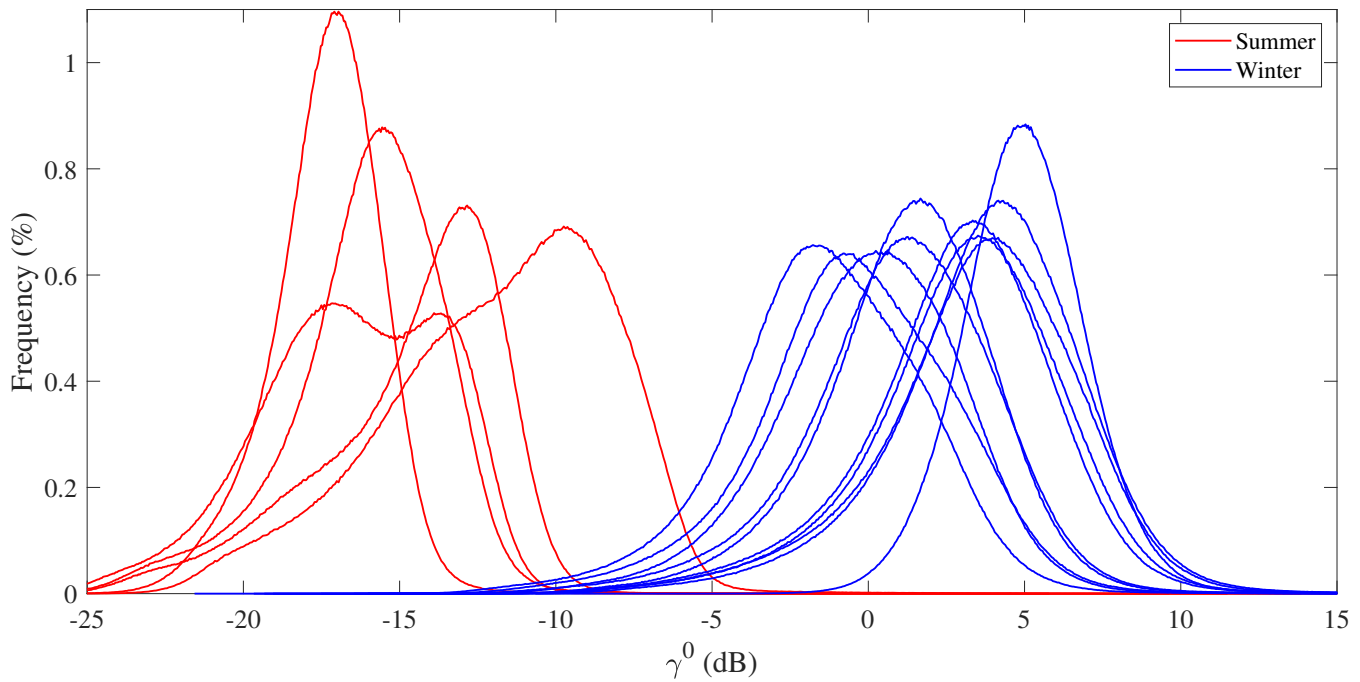


Fig. 4. Summer (red) and winter (blue) Probability Distribution Functions (PDFs) for ICEYE γ^0 values over the Helheim Fjord ice mélange matrix.

242 given that there are 4 zones compared to 2. In contrast, winter texture is more variable at a small scale
 243 as evidenced by high frequency variations that are superimposed on the lower frequency pattern of zones
 244 that we have identified.

245 Iceberg Segmentation Performance

246 Iceberg detection results for ICEYE images using the texture-based method in summer and winter are
 247 shown in Figure 6. In summer (2021; Figures 6a and 6c), the texture-based method is able to detect the
 248 large icebergs in the mélange matrix, although noise surrounding the pixels led to misclassification near
 249 their boundaries. The two icebergs near the terminus are correctly delineated, whilst the section of three
 250 icebergs further downfjord are detected although there is more noise in the detection results here. The large
 251 icebergs beyond 7 km from the terminus is correctly detected. Beyond this section, a collection of smaller
 252 icebergs have been detected, although we suspect many have been removed during the filtering process. In
 253 comparison, iceberg detection in winter (2023; Figures 6b and 6d) is of lower quality. Whilst the method
 254 correctly detects small icebergs across the matrix, it misses several of the large icebergs near the terminus.
 255 The texture analysis in the previous section demonstrated how the winter matrix has a Gaussian PDF and
 256 therefore pixel values are random. Therefore, differentiating icebergs within the mélange was not possible

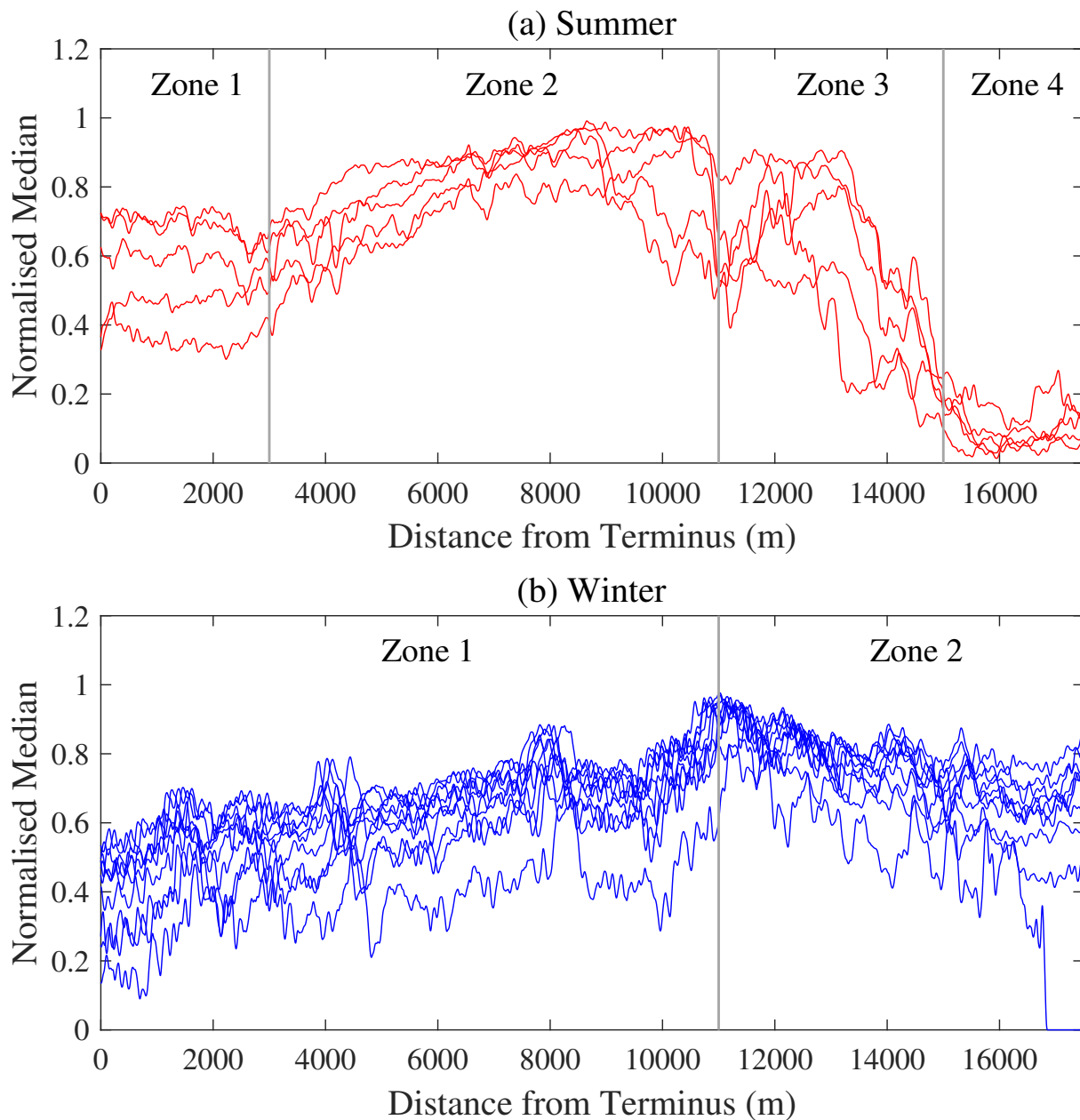


Fig. 5. The median pixel value along each column of the image in a) summer (red) and b) winter (blue). These have been normalised by dividing through by the maximum pixel value along each longitudinal profile. Manually defined zones in the profiles have been indicated.

257 based on the current texture-based detection method. It was only possible in summer due to the large
 258 variations in texture between icebergs and the surrounding mélange. In summer, large icebergs can be
 259 more readily detected whilst in winter it appears only smaller icebergs can be detected using this method.

260 ICEYE outperforms Sentinel-1 in segmenting icebergs using SAM, while both ICEYE and Sentinel-1
 261 perform similarly at segmenting the mélange matrix. Sentinel-1 correctly classified 31% and 18% of icebergs
 262 compared to our manual digitization of icebergs (Figure 7). From ICEYE images taken within 24 hours

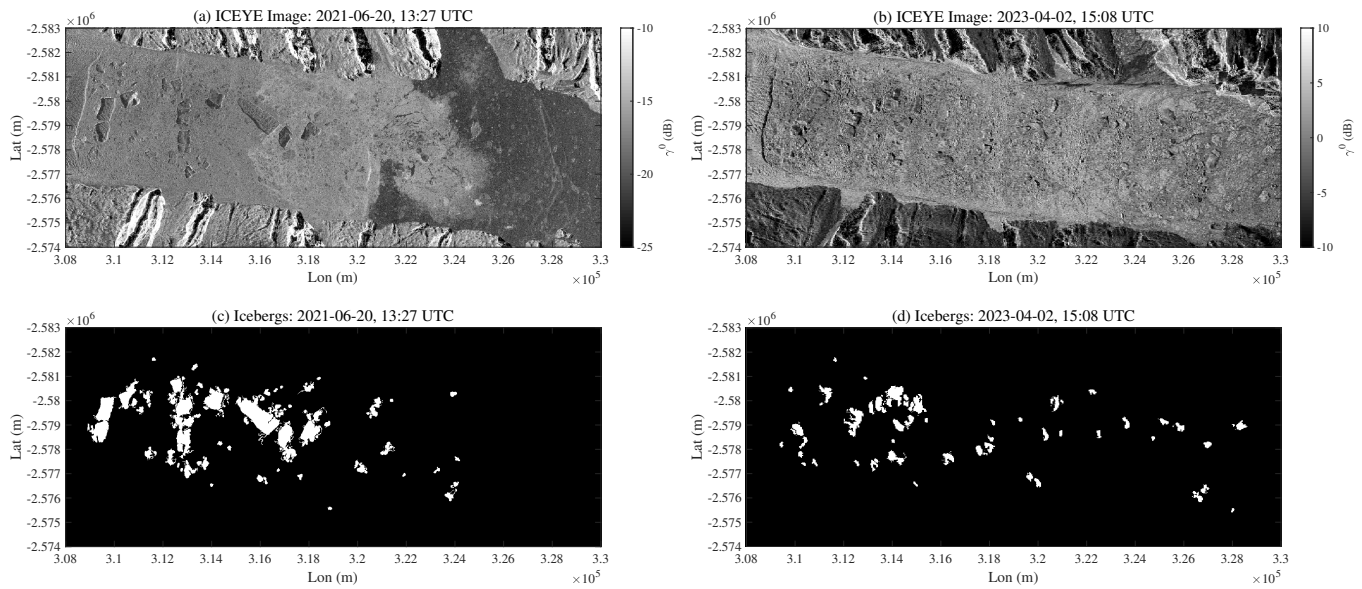


Fig. 6. Iceberg detection results using the texture-based method. The original ICEYE images in (a) summer and (b) winter are shown in the top panels, whilst the detection results are shown for (c) summer and (d) winter in the bottom panels.

263 of the Sentinel-1 images, ICEYE correctly classified 76% and 78% of icebergs. From Figure 8a, b, SAM
 264 can detect large (≥ 1 km length) icebergs in the rigid matrix accurately, while many large icebergs were
 265 undetected in the Sentinel-1 imagery (Figure 8c, d). Within the non-rigid matrix farther away from the
 266 terminus, both ICEYE and Sentinel-1 imagery misclassified small areas of sea ice as an iceberg, while a
 267 large area of sea ice in the downfjord area was misclassified in the 2023-03-08 ICEYE image (Figure 8b).
 268 Both ICEYE and Sentinel-1 are able to detect smaller icebergs, particularly in the downfjord areas, and
 269 surprisingly the 2021-06-20 Sentinel-1 image detects more smaller icebergs compared to the ICEYE image
 270 of the same date (Figures 8a, c). Sentinel-1's low and inconsistent F1 scores of 0.42 and 0.27 (Figures 7c,
 271 d) likely stem from its coarser resolution compared to ICEYE. Unlike Sentinel-1, the ICEYE F1 scores of
 272 0.76 and 0.78 (Figures 7a, b) indicate that SAM performed consistently well on ICEYE imagery.

273 Ice Mélange Velocity

274 The velocity comparison indicates that 6 out of 8 image pairs contain systematic offsets as demonstrated
 275 by the large mean values (μ) in Figure 9. For example, the velocity difference between 08-03-2023 to
 276 12-03-2023 and the ATLAS data had a mean offset of $\mu = 20.8$ m (Figure 9b), indicating a systematic
 277 offset between the two SAR images. In comparison, the mean offset between 30-03-2023 to 02-04-2023 and
 278 ATLAS was 0.2 m, indicating that the misalignment between both images was minimal. The large value

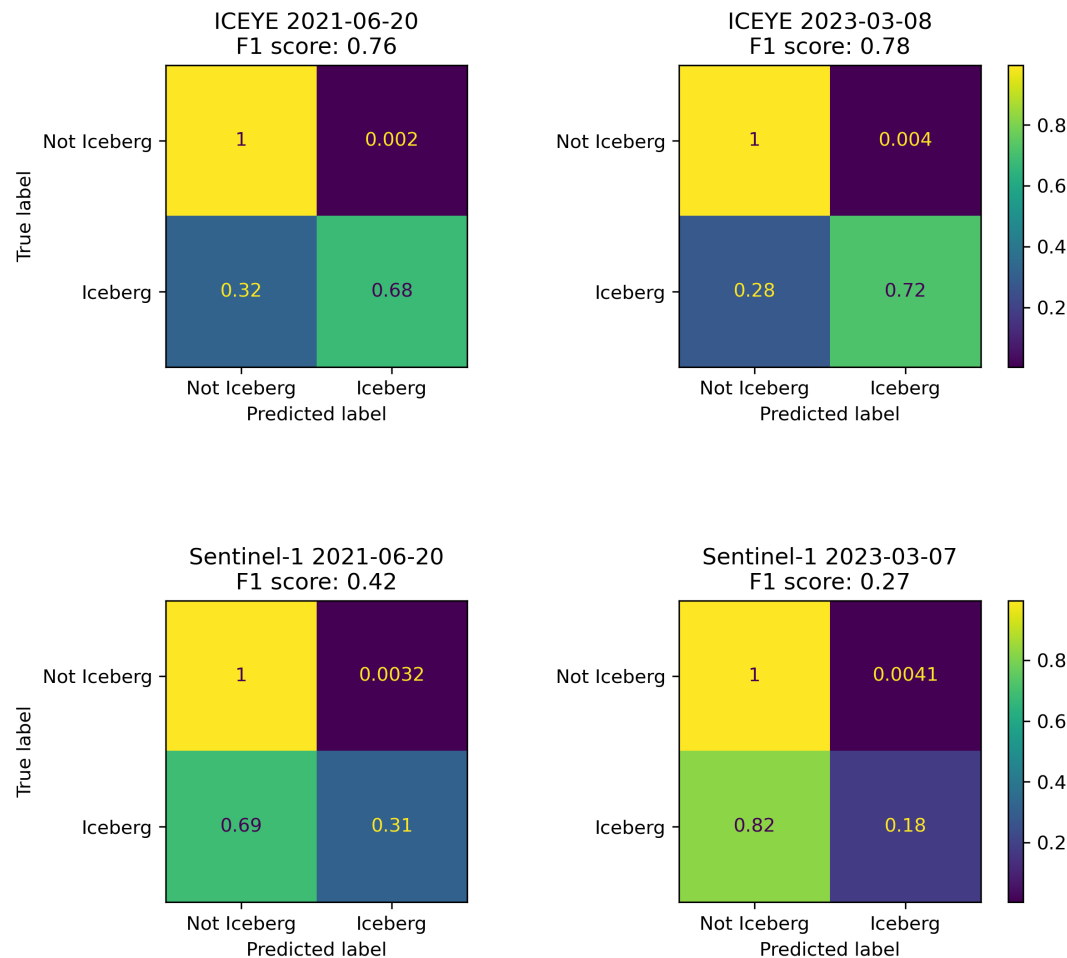


Fig. 7. Confusion matrices for ICEYE (a) summer and (b) winter and for Sentinel-1 icebergs segmentation using no prompt SAM in (c) summer and (d) 2023.

279 of μ for all but two velocity maps indicates the poor performance of ICEYE for tracking the movement
 280 of rigid ice mélange and is caused by a misalignment between the majority of the ICEYE images. In
 281 contrast, the uncertainty of each ICEYE mélange velocity map, indicated by the standard deviation (σ) of
 282 each distribution, is consistently below 5 m for 7/8 image pairs. This indicates that despite the systematic
 283 offset between the ICEYE images, the ImGRAFT feature tracking is able to compute the displacement
 284 between pixels with high accuracy. Visually, this is indicated by a narrow distribution for all histograms
 285 in Figure 9. The histograms represent the velocity of the granular matrix rather than the tracking of large
 286 icebergs because the random nature of the matrix can be tracked over time compared to the more rapidly
 287 changing iceberg surfaces. Each histogram is normally distributed, indicating the presence of random errors
 288 in the feature tracking result, illustrating that the ICEYE SAR images can sufficiently track the movement
 289 of the matrix, but the results may only be reliable if the systematic offset can be corrected.

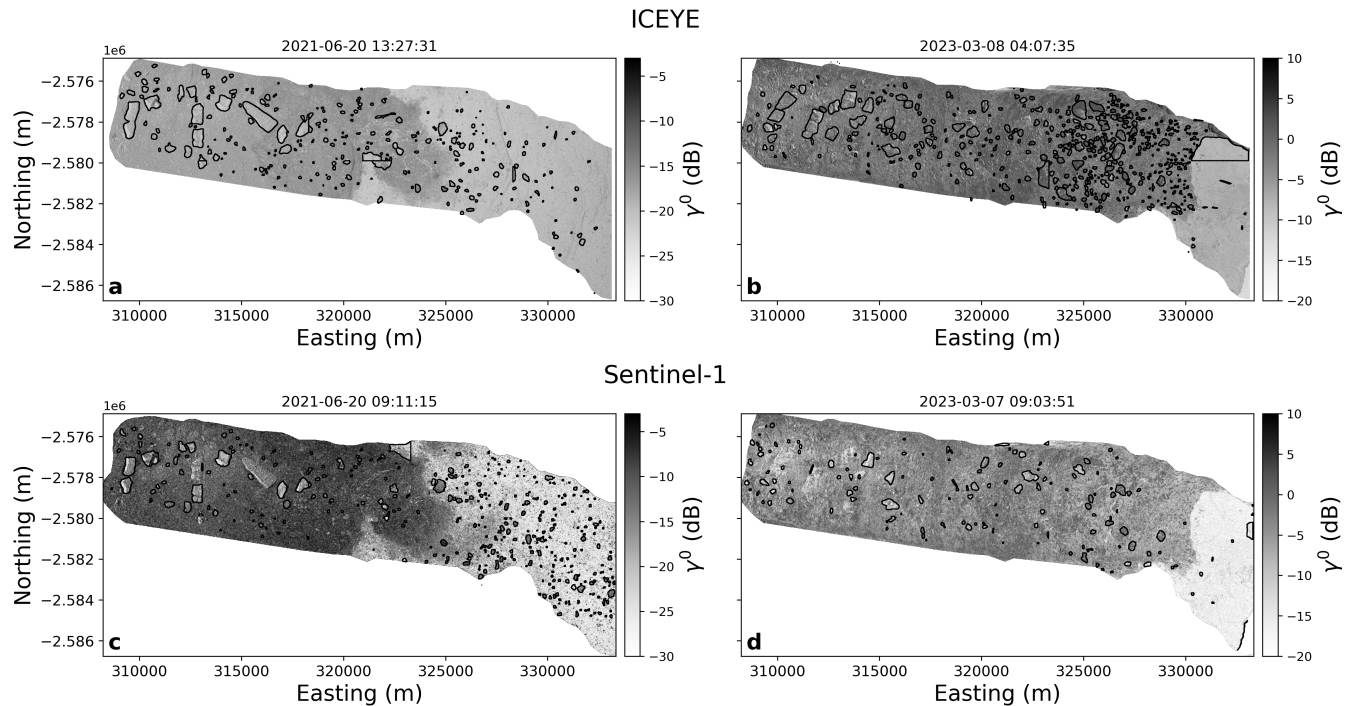


Fig. 8. Iceberg detection results using SAM. The results are overlaid on the ICEYE images in (a) summer and (b) winter. Similarly, the (c) summer and (d) winter Sentinel-1 results are shown in the bottom panel.

290 DISCUSSION

291 Performance of Ice Mélange Monitoring with ICEYE

292 This study shows that ICEYE SAR imagery can be used to measure changes in the surface characteristics of
 293 ice mélange in both summer and winter through image texture. Radar backscatter from sea ice is generally
 294 larger at X-band compared to C-band (Johansson and others, 2018) and the smaller wavelength means
 295 it is more sensitive to changes in surface conditions. This means that as the surface melts or refreezes,
 296 icebergs flip over, and new sea ice forms, ICEYE will be able to detect these changes rapidly through
 297 textural variations across the image. These changes are most apparent in summer when the non-rigid
 298 mélange melts and icebergs move around in response to fjord currents and wind patterns (Amundson and
 299 others, 2020). Air temperature at Mittivakkat glacier 80 km south of Helheim Fjord was above 0°C at the
 300 time of the summer ICEYE image acquisitions, suggesting the mélange surface may have been melting,
 301 evidenced by the negatively skewed summer distributions in Figure 4. In winter, the air temperature was -
 302 15°C , and the mélange surface was frozen; hence, radar backscatter was generally higher. This was further
 303 enhanced by the random assemblage of icebergs in the matrix evidenced by the Gaussian distribution

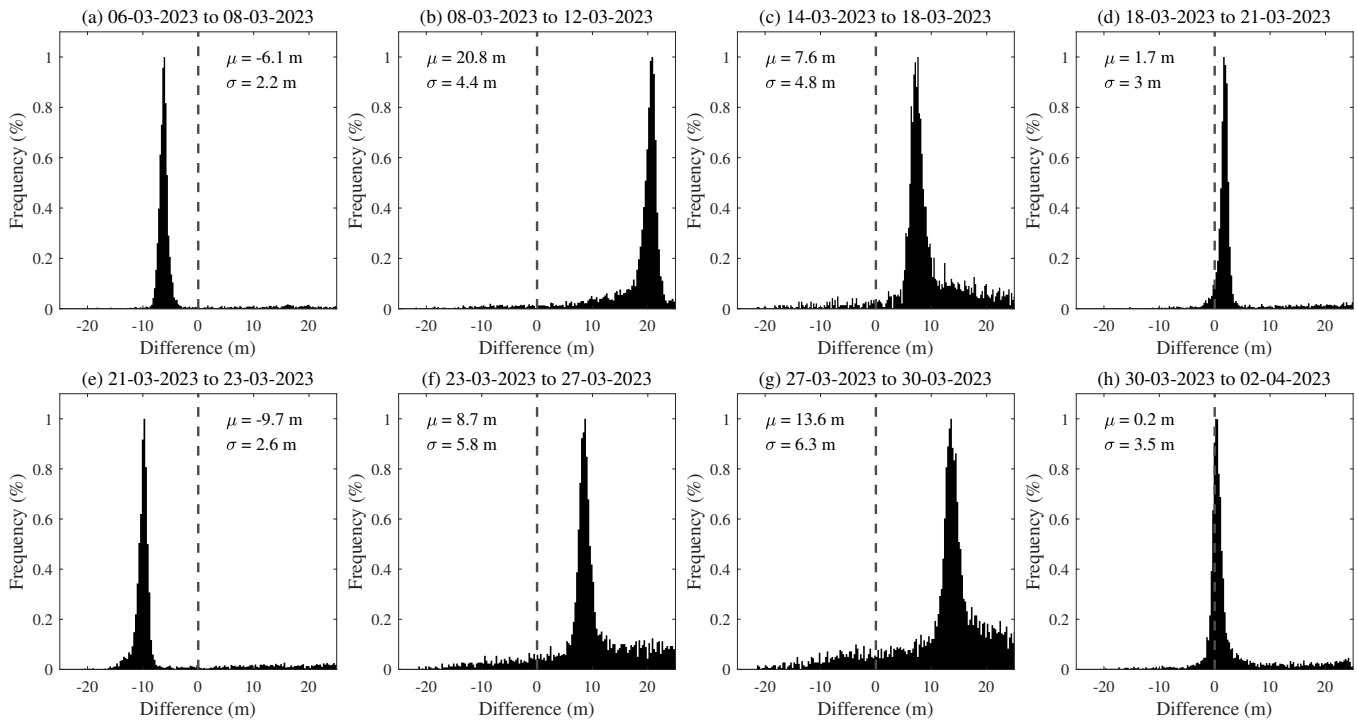


Fig. 9. Normalised histograms of the difference between ATLAS and ICEYE velocities for each of the ICEYE image pairs. Also stated for each histogram is the mean (μ) and standard deviation (σ). Black dotted line represents a mean of 0.

304 in Figure 4, which increases the mélange roughness and hence radar backscatter. Whilst this analysis
 305 may be possible with optical imagery, it cannot be used in the Polar night or under cloudy conditions.
 306 In these conditions, ICEYE is preferred over Sentinel-1 due its higher spatial resolution which enhances
 307 image textural variations and the shorter wavelength which increases the sensitivity of radar backscatter
 308 to surface changes.

309 We have also presented new techniques to segment large icebergs in the noisy mélange environment.
 310 Whilst the texture-based method is limited to working in summer when the mélange texture is more
 311 variable, SAM performs well in both seasons. Furthermore, ICEYE outperforms Sentinel-1 for iceberg
 312 segmentation which demonstrates that even with just a single polarisation, ICEYE requires less processing
 313 to achieve high classification accuracy. Previous studies have applied object-based image analysis methods,
 314 deep learning and semi-supervised clustering algorithms to SAR imagery to detect icebergs within sea ice
 315 (Mazur and others, 2017; Barbat and others, 2019; Færch and others, 2024). Shiggins and others (2023)
 316 applied a threshold to Digital Elevation Models (DEMs) to detect icebergs in the mélange, but 3D data
 317 are not widely available for routine iceberg mapping. Furthermore, dual-polarisation SAR sensors (e.g.
 318 Sentinel-1) can be used to mitigate the impact of sea surface waves which may be misclassified as icebergs,

319 hence ICEYE may not be suitable for open water iceberg detection as it only uses a single polarisation.
320 Melting icebergs increase signal absorption and icebergs that have flipped have smooth undersides which
321 increases specular reflection, hence both processes reduces radar backscatter and lead to ‘dark’ icebergs
322 with similar backscatter characteristics to open water. Both methods employed in this study were able to
323 detect these icebergs in ICEYE imagery but not in Sentinel-1, demonstrating that high-resolution imagery
324 leads to a significant improvement in detection accuracy, and with less pre-processing.

325 The geometry of the ICEYE image acquisition significantly impacts the performance of both the iceberg
326 detection algorithms and velocity retrievals. For more accurate iceberg segmentation results using SAM,
327 it is important to ensure the image patching matches the size of large icebergs, which may be >1 km in
328 length. Ensuring this will reduce the amount of times an iceberg is split between different windows, limiting
329 the artifacts produced from image patching. Furthermore, the systematic offset observed in the velocity
330 results (Figure 9) is due to the poor geolocation accuracy after range-Doppler correction when using images
331 from different orbits. Each image pair used to extract velocities contained images from different orbits,
332 even in the case of velocities with small errors (Figures 9d and 9h). This suggests that the coregistration in
333 SNAP did not sufficiently align the images to extract accurate velocities. The misalignment is due to the
334 combination of DEM and geolocation errors in both images (Kääb and others, 2016), both of which will be
335 large for the ICEYE imagery as more pixels require correction due to the high spatial resolution. This issue
336 is less severe for Sentinel-1 as their orbits are well defined and repeat images can only be from one of two
337 satellites in comparison to ICEYE. Therefore, improved methods to coregister ICEYE SAR images from
338 different orbits and viewing geometries are required to improve the velocity mapping performance over
339 both ice mélange and glaciers. This may also enable velocity mapping of ice mélange in summer, which
340 is more difficult to achieve as the matrix is non-rigid and feature-tracking results tend to be non-coherent
341 (Bevan and others, 2019).

342 **Structural Evolution of Ice Mélange**

343 The banding structure revealed by the texture analysis (e.g., Figure 5) represents changes in radar backscat-
344 ter that we suggest are due to changes in ice concentrations downfjord. In summer, the mélange matrix
345 is non-rigid and icebergs move downfjord, melting along the way due to higher atmospheric and ocean
346 temperatures, and leading to greater variations in image texture. For example, pixel values are lower
347 nearer the terminus (zone 1) where we would expect higher concentrations of medium to large icebergs. In

348 contrast, further down the fjord (zone 2), these icebergs break up into smaller fragments generating a rough
349 surface profile that increases radar backscatter at X-band (Guo and others, 2023). The lower backscatter
350 at the edge of the mélange (zone 3 in Figure 5a) relates to the increased presence of open water and sea
351 ice, both of which are smoother and consequently increase specular reflection, whilst greater surface melt
352 absorbs the ice signal. In comparison, structural bands in the winter mélange is less clear, with only a
353 single band observed. We suggest this is due to the low air temperatures and lack of surface melting, which
354 ensures the mélange remains rigid and the iceberg texture remains consistent across multiple images. The
355 presence of structural bands with distinct ice concentration properties within the mélange implies that
356 the boundary between them represents a shear plane and, therefore, lines of weakness within the granular
357 matrix. Applying this hypothesis to the winter imagery where we observe two zones and a line of weakness
358 ~ 10.1 km from the glacier terminus, we suggest that the ice mélange matrix contains structural weaknesses
359 in both seasons that may persist throughout the year.

360 The presence of shear zones within ice mélange has not been documented before and could play an
361 important role in determining the strength of the granular matrix. For example, Figure 10 shows a time
362 series of a break-up event around the time of the 2021 summer images acquired from ICEYE. No structure
363 can be observed in the optical imagery on 17th June, which is likely due to the lower contrast in ice
364 concentration at visible wavelengths. From 17th to 20th of June 2021 the mélange begins to break apart.
365 This coincides with the dates of the ICEYE imagery and confirms that the structural banding is due to
366 ice concentration differences. On 25th June, the mélange breaks up and the loose material moves down
367 fjord. At this point, the higher concentration mélange remains pinned to the large iceberg, maintaining
368 the shear plane. Then, by 27th June, most of the low-concentration mélange has dispersed, leaving behind
369 the high-concentration mélange near the terminus. This sequence serves to illustrate that the break-up
370 of the matrix initiates at the open water boundary but terminates at the shear zone created by the ice
371 concentration differences. This shortens the mélange suddenly, potentially reducing the buttressing force
372 on the tidewater glacier. Furthermore, the strong control of the high ice concentration region on the
373 mélange break-up suggests that length-width ratios (Burton and others, 2018; Schlemm and Levermann,
374 2021) might be misleading for the ‘true length’ included in backstress calculations and instead only the
375 length of the high ice concentration area should be used. The observed control of structural banding on
376 ice mélange break-up strongly implies that this event, which may occur several times across the year, may
377 be predictable if the lines of weaknesses along the shear zones can be detected. For example, they may

378 cause and define the extent of winter mélange break up events (Cassotto and others, 2015). Therefore, high
379 resolution SAR imagery from ICEYE, which can detect these subtle ice concentration differences, has the
380 necessary capabilities to monitor precursors to mélange break up which has implications for understanding
381 it's strength and buttressing force on tidewater glacier termini.

382 The presence of large icebergs at the observed shear zones within the ice mélange suggests they are
383 critical in determining the size of the structural zones and hence the strength of the matrix. In particular,
384 our iceberg detection results indicate that they stabilise in the same location in both summer and winter.
385 For example, two icebergs ~ 1 km from the terminus appear in both summer and winter and likely originate
386 from the calving of a large iceberg along the fracture lines that originate upstream of the terminus. The
387 fact these icebergs remain in the same position over 7 days in summer and in Figure 10 for 10 days suggests
388 they are pinned to a submarine sill. This appears to also be the case for the iceberg ~ 10 km from the
389 terminus which is much larger. Although direct observations of the seafloor topography are scarce, the
390 few direct observations from this region (An and others, 2019) suggest a bathymetric sill could be present
391 in the region where the largest iceberg was detected ~ 10 km from the glacier terminus. Furthermore,
392 when icebergs remain stationary they fuse sea ice together (Robel, 2017; Cassotto and others, 2021) and
393 ultimately bond the granular matrix. We therefore hypothesise that bathymetric sills represent the nucleus
394 of structural banding in the mélange by stabilising icebergs, restricting the outflow of ice and initiating sea
395 ice growth. Whilst we have observed this process directly in summer, the Gaussian PDFs in winter suggest
396 that icebergs are more randomly distributed and the structural banding is suppressed, hence further work
397 is required to understand the extent to which icebergs control the formation of shear zones in the winter
398 matrix.

399 **Future Glaciological Opportunities for ICEYE**

400 There are only a handful of studies using ICEYE to monitor glaciers, with no published studies using the
401 constellation to study icebergs or sea ice. Daily ICEYE acquisitions have been used to map grounding
402 line changes at Petermann Glacier in northern Greenland and Thwaites Glacier in Antarctica using in-
403 terferometry (Ciraci and others, 2023; Rignot and others, 2024). In both cases, the increased spatial and
404 temporal resolution, as well as an improved interferometric baseline between successive satellite passes,
405 increased the accuracy of the data products compared to satellites such as Sentinel-1. Meanwhile, Łukosz
406 and others (2021) mapped the velocity of Sermeq Kujalleq (Jakobshavn Isbræ) using an ICEYE image



Fig. 10. Ice mélange break up sequence spanning from 17th June through 27th June. Note the consistent rigid mélange shape closer to the terminus and the large tabular iceberg pinning the rigid mélange.

407 pair with a temporal separation of 4 days in winter. They suggested that the results were of a comparable
408 magnitude to Sentinel-1 velocities, but no comprehensive validation was conducted. The findings of these

409 studies suggest that ICEYE has the potential to track surface displacements across ice mélange despite the
410 poor performance of the feature-tracking reported in this study. Combined with the improved detection of
411 icebergs and the ability to monitor changes in surface characteristics, we find that ICEYE SAR imagery
412 outperforms existing satellites such as Sentinel-1 and should be considered for future monitoring of glacier
413 environments.

414 There are three key areas where the acquisition of daily ICEYE SAR images with a 2.5 spatial reso-
415 lution can deliver significant new physical understanding: 1) iceberg calving, 2) supraglacial hydrological
416 processes, and 3) glacial hazards. Firstly, ICEYE data may be employed to delineate tidewater glacier
417 termini every day as well as the crevasse fields in the terminus region, both of which are crucial features
418 in understanding calving rates and their drivers. Currently, coarse resolution satellites (Zhang and oth-
419 ers, 2023; Surawy-Stepney and others, 2023) or DEMs (Chudley and others, 2024) are used to map these
420 features, neither of which can monitor the evolution of these features. Furthermore, the resulting icebergs
421 may be tracked at higher temporal resolution, opening up the potential to infer near surface ocean currents
422 in glacial fjords. Secondly, because X-band radar backscatter from ice surfaces reduces as water content
423 increases (Ulaby and others, 2019), it follows that the improvement in spatial and temporal resolution
424 offered by ICEYE opens up the possibility to track melt patterns in greater detail than previously possible.
425 This includes the onset and spatial evolution of melt over an annual cycle, as well as the complex distri-
426 bution of supraglacial lakes and streams that form seasonally. Third and finally, several glacial hazards,
427 such as glacial lake outburst floods (GLOFs) and ice avalanches, occur suddenly in time and can have fatal
428 impacts, but only a handful are monitored by in situ instruments (Dematteis and others, 2021; Tiwari and
429 others, 2022). ICEYE SAR imagery can be used to rapidly assess glacial hazards through tasking areas
430 of interest and hence bridge the gap between ground and spaceborne monitoring. Whilst we believe there
431 are numerous future applications of ICEYE, these three areas are particularly promising and should be an
432 avenue for future development of ICEYE for cryosphere monitoring.

433 Despite the clear potential for using ICEYE for ice mélange and glacier monitoring, there are technical
434 challenges that must be overcome. The orbits of each ICEYE satellite is different, therefore terrain dis-
435 tortions introduced by the side-looking SAR geometry varies between each satellite. Developing correction
436 algorithms that effectively remove terrain distortions and accurately geocodes the resulting image, then
437 fully validating these approaches, is crucial for exploiting the dense time series of observations that can
438 be acquired through the ICEYE constellation. This is particularly important across ice mélange where a

439 DEM matching the SAR image acquisition time is usually not available. Coregistering SAR images for
440 feature-tracking is a related issue, and we found in this study that coregistration using SNAP performed
441 poorly, leading to large errors in the resulting velocity fields. Therefore, concurrently with the improve-
442 ments in geometric image corrections, improved coregistration of ICEYE SAR images should be developed
443 to enable more accurate velocity mapping. Furthermore, ICEYE uses a single polarisation which reduces
444 the diversity of information it can measure. This was observed when differentiating between large icebergs
445 and the surrounding mélange in winter where the pixel values of the co-polarised backscatter did not vary
446 significantly to enable the differentiation of each using the texture-based segmentation method. In this
447 study, we use GLCM texture layers to enhance iceberg segmentation, but other texture-based methods such
448 as Gabor transforms, wavelet transforms or edge detectors (Kandaswamy and others, 2005) or phase-based
449 RGB composites (Arenas-Pingarrón and others, 2023) may help to improve the classification and segmen-
450 tation of ice mélange image features. Finally, the texture-based iceberg segmentation method should be
451 developed in the future as a tool to automatically label icebergs as training data (pseudo-labeling) for deep
452 learning algorithms such as SAM to reduce the need for manual intervention in the training process.

453 CONCLUSIONS

454 In this study, we have used high-resolution ICEYE SAR imagery to map the dynamics of ice mélange
455 in Greenland by mapping image texture, segmenting icebergs in the noisy mélange environment, and
456 tracking the velocity of the matrix. Texture analysis reveals banding within the mélange that relates
457 to changes in ice concentrations downfjord. This structure is partially due to the stabilisation of large
458 icebergs, potentially on submarine sills, which then act as the nucleus of sea ice formation whilst also
459 preventing the downfjord flow of smaller icebergs. This structure creates shear zones within the matrix,
460 and we show through a sequence of optical satellite images that the mélange breaks up along these lines of
461 weakness through calving. The fact that this structure is present in both summer and winter suggests the
462 mélange is susceptible to break-up throughout the year. Furthermore, we find that ICEYE outperforms
463 Sentinel-1 when segmenting large icebergs in the mélange using the deep learning model SAM (Kirillov
464 and others, 2023), suggesting that high resolution SAR imagery improves iceberg monitoring. In contrast,
465 poor coregistration between ICEYE images in different orbits leads to errors in velocity maps, rendering
466 them unusable for tracking the dynamics of the mélange. Improved algorithms for image registration
467 are required to develop ICEYE for monitoring ice mélange and glacier flow rates. Overall, the ability to

468 acquire 2.5 m resolution SAR images at daily or subdaily resolution with large image swaths enables more
469 detailed monitoring of highly dynamic processes and has the potential to be used in a range of glaciological
470 applications e.g. hazard monitoring, understanding iceberg calving.

471 ACKNOWLEDGEMENTS

472 We acknowledge funding to purchase ICEYE images in 2021 from the Scottish Alliance for Geoscience, En-
473 vironment and Society (SAGES) International Collaboration Scheme (SICS) and access to ICEYE imagery
474 in 2023 through the European Space Agency (ESA) Third Party Mission (TPM) scheme (Proposal ID:
475 PP0089920). Leigh Stearns and Michael Shahin acknowledge funding from the Heising-Simons Foundation
476 (HSF #2017-316) and NSF (BAA #00124801).

477 REFERENCES

- 478 Amundson JM and Burton J (2018) Quasi-static granular flow of ice mélange. *Journal of Geophysical Research:*
479 *Earth Surface*, **123**(9), 2243–2257
- 480 Amundson JM, Fahnestock M, Truffer M, Brown J, Lüthi MP and Motyka RJ (2010) Ice mélange dynamics and
481 implications for terminus stability, jakobshavn isbræ, greenland. *Journal of Geophysical Research: Earth Surface*,
482 **115**(F1)
- 483 Amundson JM, Kienholz C, Hager AO, Jackson RH, Motyka RJ, Nash JD and Sutherland DA (2020) Formation,
484 flow and break-up of ephemeral ice mélange at leconte glacier and bay, alaska. *Journal of Glaciology*, **66**(258),
485 577–590
- 486 An L, Rignot E, Chauche N, Holland DM, Holland D, Jakobsson M, Kane E, Wood M, Klaucke I, Morlighem M and
487 others (2019) Bathymetry of southeast greenland from oceans melting greenland (omg) data. *Geophysical Research*
488 *Letters*, **46**(20), 11197–11205
- 489 Arenas-Pingarrón Á, Corr HF, Brennan PV, Robinson C, Jordan TA, Brisbourne A and Martín C (2023) New repre-
490 sentation of synthetic aperture radar images for enhanced ice-sounding interpretation. In *EGU General Assembly*
491 *Conference Abstracts*, EGU–2856
- 492 Barbat MM, Wesche C, Werhli AV and Mata MM (2019) An adaptive machine learning approach to improve auto-
493 matic iceberg detection from sar images. *ISPRS Journal of Photogrammetry and Remote Sensing*, **156**, 247–259
- 494 Bevan SL, Luckman AJ, Benn DI, Cowton T and Todd J (2019) Impact of warming shelf waters on ice mélange and
495 terminus retreat at a large se greenland glacier. *The Cryosphere*, **13**(9), 2303–2315 (doi: 10.5194/tc-13-2303-2019)

- 496 Burton JC, Amundson JM, Cassotto R, Kuo CC and Dennin M (2018) Quantifying flow and stress in ice mélange,
497 the world's largest granular material. *Proceedings of the National Academy of Sciences*, **115**(20), 5105–5110
- 498 Cassotto R, Fahnestock M, Amundson JM, Truffer M and Joughin I (2015) Seasonal and interannual variations in ice
499 mélange and its impact on terminus stability, jakobshavn isbræ, greenland. *Journal of Glaciology*, **61**(225), 76–88
- 500 Cassotto RK, Burton JC, Amundson JM, Fahnestock MA and Truffer M (2021) Granular decoherence precedes ice
501 mélange failure and glacier calving at jakobshavn isbræ. *Nature Geoscience*, **14**(6), 417–422
- 502 Chudley TR, Howat IM, King MD and MacKie E (2024) Increased crevassing across accelerating greenland ice sheet
503 margins. *PREPRINT (Version 1) available at EarthArxiv* (doi: <https://doi.org/10.31223/X58099>)
- 504 Ciraci E, Rignot E, Scheuchl B, Tolpekin V, Wollersheim M, An L, Milillo P, Bueso-Bello JL, Rizzoli P and Dini
505 L (2023) Melt rates in the kilometer-size grounding zone of petermann glacier, greenland, before and during a
506 retreat. *Proceedings of the National Academy of Sciences*, **120**(20), e2220924120
- 507 Cook S, Rutt I, Murray T, Luckman A, Zwinger T, Selmes N, Goldsack A and James T (2014) Modelling environ-
508 mental influences on calving at helheim glacier in eastern greenland. *The Cryosphere*, **8**(3), 827–841
- 509 Davison B, Cowton T, Cottier FR and Sole A (2020) Iceberg melting substantially modifies oceanic heat flux towards
510 a major greenlandic tidewater glacier. *Nature communications*, **11**(1), 5983
- 511 Dematteis N, Giordan D, Troilo F, Wrzesniak A and Godone D (2021) Ten-year monitoring of the grandes jorasses
512 glaciers kinematics. limits, potentialities, and possible applications of different monitoring systems. *Remote Sensing*,
513 **13**(15), 3005
- 514 Everett A, Murray T, Selmes N, Holland D and Reeve DE (2021) The impacts of a subglacial discharge plume on
515 calving, submarine melting, and mélange mass loss at helheim glacier, south east greenland. *Journal of Geophysical*
516 *Research: Earth Surface*, **126**(3), e2020JF005910
- 517 Færch L, Dierking W, Hughes N and Doulgeris AP (2024) Mapping icebergs in sea ice: An analysis of seasonal sar
518 backscatter at c-and l-band. *Remote Sensing of Environment*, **304**, 114074
- 519 Foga S, Stearns LA and Van der Veen C (2014) Application of satellite remote sensing techniques to quantify terminus
520 and ice mélange behavior at helheim glacier, east greenland. *Marine Technology Society Journal*, **48**(5), 81–91
- 521 Fried M, Catania G, Stearns L, Sutherland D, Bartholomaus T, Shroyer E and Nash J (2018) Reconciling drivers
522 of seasonal terminus advance and retreat at 13 central west greenland tidewater glaciers. *Journal of Geophysical*
523 *Research: Earth Surface*, **123**(7), 1590–1607

- 524 Guo W, Itkin P, Singha S, Doulgeris AP, Johansson M and Spreen G (2023) Sea ice classification of terrasars-x
525 scansar images for the mosaic expedition incorporating per-class incidence angle dependency of image texture.
526 *The Cryosphere*, **17**(3), 1279–1297 (doi: 10.5194/tc-17-1279-2023)
- 527 Haralick RM, Shanmugam K and Dinstein IH (1973) Textural features for image classification. *IEEE Transactions*
528 *on systems, man, and cybernetics*, **6**, 610–621
- 529 Howat IM, Box JE, Ahn Y, Herrington A and McFADDEN EM (2010) Seasonal variability in the dynamics of
530 marine-terminating outlet glaciers in greenland. *Journal of Glaciology*, **56**(198), 601–613
- 531 ICEYE (2023) Iceye missions brochure. Technical report, ICEYE
- 532 Johansson AM, Brekke C, Spreen G and King JA (2018) X-, c-, and l-band sar signatures of newly formed sea ice in
533 arctic leads during winter and spring. *Remote Sensing of Environment*, **204**, 162–180
- 534 Kääb A, Winsvold SH, Altena B, Nuth C, Nagler T and Wuite J (2016) Glacier remote sensing using sentinel-2. part
535 i: Radiometric and geometric performance, and application to ice velocity. *Remote sensing*, **8**(7), 598
- 536 Kandaswamy U, Adjeroh DA and Lee MC (2005) Efficient texture analysis of sar imagery. *IEEE Transactions on*
537 *Geoscience and Remote Sensing*, **43**(9), 2075–2083
- 538 Kirillov A, Mintun E, Ravi N, Mao H, Rolland C, Gustafson L, Xiao T, Whitehead S, Berg AC, Lo WY, Dollár P
539 and Girshick R (2023) Segment anything
- 540 Łukosz MA, Hejmanowski R and Witkowski WT (2021) Evaluation of iceye microsattellites sensor for surface motion
541 detection—jakobshavn glacier case study. *Energies*, **14**(12), 3424
- 542 Mankoff KD, Colgan W, Solgaard A, Karlsson NB, Ahlstrøm AP, van As D, Box JE, Khan SA, Kjeldsen KK,
543 Mougnot J and Fausto RS (2019) Greenland ice sheet solid ice discharge from 1986 through 2017. *Earth System*
544 *Science Data*, **11**(2), 769–786 (doi: 10.5194/essd-11-769-2019)
- 545 Marochov M, Stokes CR and Carbonneau PE (2021) Image classification of marine-terminating outlet glaciers in
546 greenland using deep learning methods. *The Cryosphere*, **15**(11), 5041–5059
- 547 Mazur A, Wåhlin AK and Krężel A (2017) An object-based sar image iceberg detection algorithm applied to the
548 amundsen sea. *Remote Sensing of Environment*, **189**, 67–83
- 549 Messerli A and Grinsted A (2015) Image georectification and feature tracking toolbox: Imgraft. *Geoscientific Instru-*
550 *mentation, Methods and Data Systems*, **4**(1), 23–34
- 551 Miles VV, Miles MW and Johannessen OM (2016) Satellite archives reveal abrupt changes in behavior of helheim
552 glacier, southeast greenland. *Journal of Glaciology*, **62**(231), 137–146

- 553 Moon T, Joughin I and Smith B (2015) Seasonal to multiyear variability of glacier surface velocity, terminus position,
554 and sea ice/ice mélange in northwest greenland. *Journal of Geophysical Research: Earth Surface*, **120**(5), 818–833
- 555 Mouginot J, Rignot E, Björk AA, Van den Broeke M, Millan R, Morlighem M, Noël B, Scheuchl B and Wood M
556 (2019) Forty-six years of greenland ice sheet mass balance from 1972 to 2018. *Proceedings of the national academy
557 of sciences*, **116**(19), 9239–9244
- 558 Moyer A, Sutherland D, Nienow P and Sole A (2019) Seasonal variations in iceberg freshwater flux in sermilik fjord,
559 southeast greenland from sentinel-2 imagery. *Geophysical Research Letters*, **46**(15), 8903–8912
- 560 Muff D, Ignatenko V, Dogan O, Lamentowski L, Leprovost P, Nottingham M, Radius A, Seilonen T and Tolpekin
561 V (2022) The iceye constellation-some new achievements. In *2022 IEEE Radar Conference (RadarConf22)*, 1–4,
562 IEEE
- 563 Otosaka IN, Shepherd A, Ivins ER, Schlegel NJ, Amory C, van den Broeke MR, Horwath M, Joughin I, King
564 MD, Krinner G, Nowicki S, Payne AJ, Rignot E, Scambos T, Simon KM, Smith BE, Sørensen LS, Velicogna I,
565 Whitehouse PL, A G, Agosta C, Ahlstrøm AP, Blazquez A, Colgan W, Engdahl ME, Fettweis X, Forsberg R,
566 Gallée H, Gardner A, Gilbert L, Gourmelen N, Groh A, Gunter BC, Harig C, Helm V, Khan SA, Kittel C, Konrad
567 H, Langen PL, Lecavalier BS, Liang CC, Loomis BD, McMillan M, Melini D, Mernild SH, Mottram R, Mouginot
568 J, Nilsson J, Noël B, Pattle ME, Peltier WR, Pie N, Roca M, Sasgen I, Save HV, Seo KW, Scheuchl B, Schrama
569 EJO, Schröder L, Simonsen SB, Slater T, Spada G, Sutterley TC, Vishwakarma BD, van Wessem JM, Wiese D,
570 van der Wal W and Wouters B (2023) Mass balance of the greenland and antarctic ice sheets from 1992 to 2020.
571 *Earth System Science Data*, **15**(4), 1597–1616 (doi: 10.5194/essd-15-1597-2023)
- 572 Otsu N (1979) A threshold selection method from gray-level histograms. *IEEE transactions on systems, man, and
573 cybernetics*, **9**(1), 62–66
- 574 Peters IR, Amundson JM, Cassotto R, Fahnestock M, Darnell KN, Truffer M and Zhang WW (2015) Dynamic
575 jamming of iceberg-choked fjords. *Geophysical Research Letters*, **42**(4), 1122–1129
- 576 Rignot E, Ciraci E, Scheuchl B, Tolpekin V, Wollersheim M and Dow C (2024) Widespread seawater intrusions
577 beneath the grounded ice of thwaites glacier, west antarctica. *Proceedings of the National Academy of Sciences*,
578 **121**(22), e2404766121
- 579 Robel AA (2017) Thinning sea ice weakens buttressing force of iceberg mélange and promotes calving. *Nature
580 Communications*, **8**(1), 14596
- 581 Schlemm T and Levermann A (2021) A simple parametrization of mélange buttressing for calving glaciers. *The
582 Cryosphere*, **15**(2), 531–545 (doi: 10.5194/tc-15-531-2021)

- 583 Shahin M (in prep) Tbc. *TBC*
- 584 Shankar S, Stearns LA and van der Veen C (2023) Semantic segmentation of glaciological features across multiple
585 remote sensing platforms with the segment anything model (sam). *Journal of Glaciology*, 1–10
- 586 Shepherd A, Ivins E, Rignot E, Smith B, van den Broeke M, Velicogna I, Whitehouse P, Briggs K, Joughin I, Krinner
587 G, Nowicki S, Payne T, Scambos T, Schlegel N, A G, Agosta C, Ahlstrøm A, Babonis G, Barletta VR, Bjørk AA,
588 Blazquez A, Bonin J, Colgan W, Csatho B, Cullather R, Engdahl ME, Felikson D, Fettweis X, Forsberg R, Hogg
589 AE, Gallee H, Gardner A, Gilbert L, Gourmelen N, Groh A, Gunter B, Hanna E, Harig C, Helm V, Horvath A,
590 Horwath M, Khan S, Kjeldsen KK, Konrad H, Langen PL, Lecavalier B, Loomis B, Luthcke S, McMillan M, Melini
591 D, Mernild S, Mohajerani Y, Moore P, Mottram R, Mouginot J, Moyano G, Muir A, Nagler T, Nield G, Nilsson
592 J, Noël B, Ootosaka I, Pattle ME, Peltier WR, Pie N, Rietbroek R, Rott H, Sandberg Sørensen L, Sasgen I, Save
593 H, Scheuchl B, Schrama E, Schröder L, Seo KW, Simonsen SB, Slater T, Spada G, Sutterley T, Talpe M, Tarasov
594 L, van de Berg WJ, van der Wal W, van Wessem M, Vishwakarma BD, Wiese D, Wilton D, Wagner T, Wouters
595 B, Wuite J and Team TI (2020) Mass balance of the greenland ice sheet from 1992 to 2018. *Nature*, **579**(7798),
596 233–239, ISSN 1476-4687 (doi: 10.1038/s41586-019-1855-2)
- 597 Shiggins CJ, Lea JM and Brough S (2023) Automated arcticdem iceberg detection tool: insights into area and volume
598 distributions, and their potential application to satellite imagery and modelling of glacier–iceberg–ocean systems.
599 *The Cryosphere*, **17**(1), 15–32
- 600 Simonsen SB, Barletta VR, Colgan WT and Sørensen LS (2021) Greenland ice sheet mass balance (1992–2020) from
601 calibrated radar altimetry. *Geophysical Research Letters*, **48**(3), e2020GL091216
- 602 Surawy-Stepney T, Hogg AE, Cornford SL and Hogg DC (2023) Mapping antarctic crevasses and their evolution with
603 deep learning applied to satellite radar imagery. *The Cryosphere*, **17**(10), 4421–4445 (doi: 10.5194/tc-17-4421-2023)
- 604 Tiwari A, Sain K, Kumar A, Tiwari J, Paul A, Kumar N, Haldar C, Kumar S and Pandey CP (2022) Potential
605 seismic precursors and surficial dynamics of a deadly himalayan disaster: An early warning approach. *Scientific*
606 *reports*, **12**(1), 3733
- 607 Ulaby F, Dobson MC and Álvarez-Pérez JL (2019) *Handbook of radar scattering statistics for terrain*. Artech House
- 608 Wehrlé A, Lüthi MP and Vieli A (2023) The control of short-term ice mélange weakening episodes on calving activity
609 at major greenland outlet glaciers. *The Cryosphere*, **17**(1), 309–326
- 610 Xie S, Dixon TH, Holland DM, Voytenko D and Vaňková I (2019) Rapid iceberg calving following removal of tightly
611 packed pro-glacial mélange. *Nature communications*, **10**(1), 3250

612 Zhang E, Catania G and Trugman DT (2023) Autoterm: an automated pipeline for glacier terminus extraction using
613 machine learning and a “big data” repository of greenland glacier termini. *The Cryosphere*, **17**(8), 3485–3503 (doi:
614 10.5194/tc-17-3485-2023)